Journal of Materials Chemistry A

ROYAL SOCIETY OF CHEMISTRY

PAPER

View Article Online
View Journal

Cite this: DOI: 10.1039/d6ta02188c

The role of precursor decomposition in low-temperature solution-based synthesis and crystallization of Li-garnet solid electrolyte films

Lucie Quincke, [a] Gaurav Anand,[a] Farheen N. Sayed, [bc] Clare P. Grey, [bc] Barbara A. J. Lechner [a] and Jennifer L. M. Rupp *[ade]

A key challenge for incorporation of oxide-based solid electrolytes into batteries remains the brittle nature of the ceramic, which makes scalable, low-cost fabrication of thin (<20 μm) separators challenging. solution-based processing, involving the direct liquid-to-solid transformation of a precursor solution into a ceramic film through deposition and annealing, offers an attractive route to overcome these fabrication challenges while significantly reducing processing temperatures compared to conventional solid-state methods. However, the relationship between the initial choices made in precursor chemistries and the crystallization behavior remains poorly understood, limiting control over the phase formation process. Here, we investigate how the precursor decompositions influence the structure evolution during annealing and crystallization of solution-processed Li-garnet solid electrolyte films. The results reveal a sequence of solvent and precursor decompositions with the Li-precursor, $LiNO_3$, decomposition occurring last and in parallel with the nucleation of $La_2Zr_2O_7$ as the first crystalline metal-oxide phase. Upon Li-precursor decomposition, the latter is lithiated to form the desired highly conductive cubic $Li_{6.25}Al_{0.25}La_3Zr_2O_{12}$ phase. This simultaneity of crystallization and decomposition events demonstrates the importance of the initial precursor choices to control the crystallization process. Through this work, we contribute to fundamental ceramic materials science by establishing a systematic methodology for studying solution-processing and providing a foundation for future precursor design of next-generation solid electrolyte battery components.

Received 13th March 2026
Accepted 13th May 2026

DOI: 10.1039/d6ta02188c

rsc.li/materials-a

Introduction

The ongoing electrification of transportation requires advanced energy storage options for increasing the driving range of electric vehicles. New battery designs and materials are needed that enable higher energy densities compared to the conventional lithium-ion batteries. Next generation, hybrid or all-solid-state, batteries offer improvements in safety and energy density by incorporating non-flammable electrolytes as solids, which are stable towards lithium metal or silicon as anode materials. Oxide-based ceramic solid electrolytes, such as Li-garnets, $Li_{6.25}Al_{0.25}La_3Zr_2O_{12}$ (LLZO), offer a high ionic conductivity, 10^{-3} to 10^{-4} S cm^{-1}, and stability against lithium metal anodes.[1–3] Besides these advantages, the major challenge for bringing oxide based solid electrolytes to the market is to reduce their manufacturing costs,[4] make the manufacturing roll-to-roll compatible and access a thickness range of below 20 μm to enable competitive energy densities.[5–7] To date, ionic conductivity and battery performance values are in their majority obtained from macrocrystalline LLZO in the form of pressed pellets or tapes, for which the initial powders have been synthesized by solid-state reaction.[8] This process includes the synthesis of the desired phase through mixing of precursors and calcination at high temperature (Fig. 1 and Table 1). As alternative to the solid-state reaction, approaches such as, amongst others, solution-based combustion synthesis or sol–gel can be used to fabricate ceramic nano-powders at reduced calcination temperatures.[9–11] Either way, tapes or pellets are then formed as green bodies from the synthetized ceramic powder through slurry-coating or cold-pressing, respectively, and are sintered at temperatures above 1050 °C for densification resulting in grain sizes of at least several microns.[12,13] This process is limited in its ability to meet the market needs described previously, due to too high processing temperatures and many processing steps that make the manufacturing expensive, while also not being roll-to-roll compatible.

[a]Department of Chemistry, TUM School of Natural Sciences, Technical University of Munich, Lichtenbergstr. 4, 85748 Garching, Germany. E-mail: jrupp@tum.de
[b]Yusuf Hamied Department of Chemistry, University of Cambridge, Lensfield Road, Cambridge CB2 1EW, UK
[c]The Faraday Institution, Harwell Science and Innovation Campus, Didcot OX11 0RA, UK
[d]TUMint.Energy Research GmbH, Lichtenbergstr. 4, Garching, Germany
[e]Fritz-Haber-Institut of the Max-Planck-Society, Faradayweg 4-6, 14195 Berlin, Germany

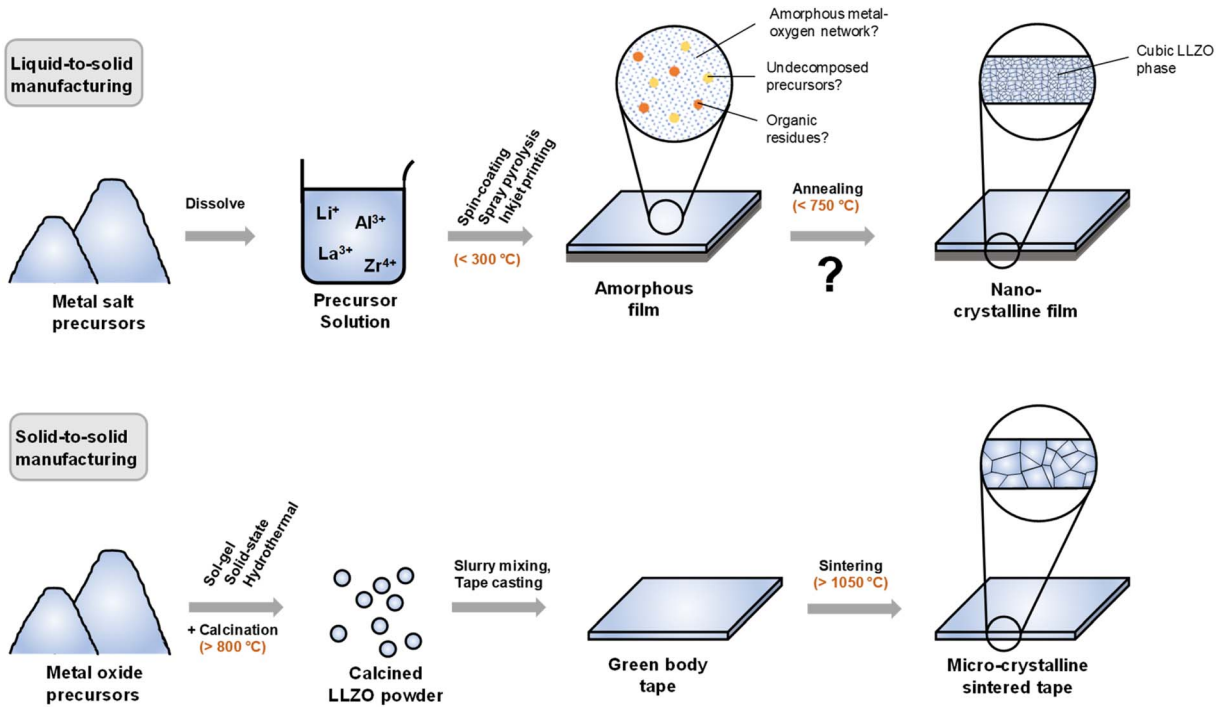

Fig. 1 Comparison of liquid-to-solid and solid-to-solid manufacturing of oxide based ceramic solid electrolytes. Liquid-to-solid manufacturing enables the scalable fabrication of dense and homogenous films with a higher aspect ratio of grain size to thickness and requires lower processing temperatures compared to classic solid-to-solid manufacturing of freestanding tapes.

Furthermore, reaching thicknesses of tapes of below 50 μm remains challenging because the small aspect ratio of tape thickness to average grain size poses challenges to mechanical stability and electrochemical performance,[14] and chemical instability with cathode materials in composite cathodes or the crucible materials can result in secondary phase formation, decomposition and compositional changes at high sintering temperatures.[15,16] Neither can vacuum-based synthesis techniques such as pulsed laser deposition meet the market needs, as they are also too expensive while not being scalable.[4] Solution-based film fabrication is the most promising approach to meet all these requirements (Fig. 1 and Table 1). It can be transferred to a roll-to-roll process and enables the fabrication of cost-efficient solid electrolytes while accessing a competitive thickness range of 1–10 μm.[4,17] Furthermore, processing temperatures of below 750 °C significantly reduce the thermal budget of solid electrolyte manufacturing, having a large impact on reducing greenhouse gas emissions during ceramic manufacturing, see recent ref. 18 for details.

In general, solution-based processing of oxide ceramic films is a well-established process which comprises four main steps: (I) preparation of a homogenous solution containing all metal cations in stoichiometric ratios, (II) deposition of the solution onto a substrate, followed by a thermal treatment for (III) the pyrolysis of precursors or organic compounds initiating the condensation to form an amorphous metal–oxygen network, and (IV) the crystallization of the final ceramic material.[19] The preparation of a homogenous solution is usually achieved by dissolving either metal alkoxides (sol–gel process) or soluble inorganic metal salts (often nitrates) in aqueous or alcohol

Table 1 Comparison of properties of oxide-based ceramic electrolytes: films fabricated *via* liquid-to-solid and tapes *via* solid-to-solid manufacturing[4,17,31–33]

	Liquid-to-solid manufacturing (films)	Solid-to-solid manufacturing (tapes)
Thickness	1–10 μm	>50 μm
Grain size	Nanometer	Micrometer
Aspect ratio (thickness to grain size)	>100	10–50
Geometry	Substrate based	Freestanding or substrate based
Roll-to-roll compatibility	Yes	No (in case of classic sintering)
Precursor type	Metal salts	Metal oxides
Maximum processing temperature for cubic LLZO phase	750 °C, 15 min to 500 °C, 10 h	>1050 °C, multiple hours and steps
Densification mechanism	Nucleation and growth from an amorphous state	Grain boundary and volume diffusion through sintering

based solutions while the most commonly used deposition methods include spin-, slot-die-, or dip-coating, inkjet printing and spray-coating. One of the major advantages of solution-based film fabrication is the simultaneous phase formation and densification following a single nucleation and growth step at much lower temperatures compared to conventional solid-state synthesis. Furthermore, there is no need of tape casting and sintering. Due to the direct transition from liquid to film state, the stoichiometry of the compounds can be easily controlled and losses, *e.g.* due to lithium evaporation at high sintering temperatures, are significantly reduced. This becomes especially important when considering solution-based synthesis of solid electrolyte materials for lithium metal batteries. After annealing, dense ceramic films with thicknesses of below 1 μm (spin-coating) and 1–10 μm (spray pyrolysis) in amorphous or nanocrystalline structure are reported, depending on the final annealing temperature.[17,20,21] If in a crystalline state, these films can reach an aspect ratio of thickness to average grain size of >100–1000, with average grain sizes of 10–100 nm, which is significantly higher than those obtained *via* solid-state synthesis.[17]

Very few studies exist that investigate solution-processed LLZO films.[7] These involve the preparation of precursor solutions which are used to deposit films *via* spin-coating,[20,22–25] dip-coating,[26,27] inkjet printing,[28] or spray pyrolysis.[17,21] Different kinds of precursor solution are designed for these synthesis protocols, depending on the choice of precursor salts and solvents. A classic sol is formed, when metal alkoxides are dissolved in organic solvents and water is added to initiate the hydrolysis of the precursors, resulting in a colloidal dispersion.[23] On the other hand, a solution is obtained when inorganic salts, mostly nitrates and/or organic salts, are dissolved in organic solvents without undergoing hydrolysis and nanoparticle growth steps.[17] However, there is no clear separation between these two solution types and in literature, mostly mixtures of solution-forming nitrates and sol-forming alkoxides, optionally further combined with chelating agents or in microemulsions are used for solution-processed LLZO thin films. After deposition of the films, annealing at intermediate temperatures, up to 600 °C, results in the preservation of an amorphous network with pyrochlore $La_2Zr_2O_7$ (LZO) crystallites, while higher temperatures, excess lithium and control of atmosphere and heating rates are required to obtain cubic LLZO (cLLZO) at temperatures of 600–800 °C.[20,22,24–28] Besides this, little knowledge exists regarding the formation mechanism of the final nanocrystalline ceramic film during annealing. Previously, high resolution transmission electron microscopy (HR-TEM) on solution-processed LLZO films revealed the formation of LZO nuclei from the amorphous metal–oxygen network, which transform upon lithiation into tetragonal LLZO (tLLZO) as crystalline intermediate before obtaining the highly conductive cubic LLZO phase at 750 °C.[21] Furthermore, significant effort was made to elucidate the structure of the amorphous La–Zr–O network identifying La as network modifier and Zr as network former.[29] However, the influence of the solvents and metal precursors on the structure evolution of the as-deposited LLZO films or at low annealing temperatures, and the role of the Li salt precursor on the onset of lithiation of the LZO phase to form LLZO remain unclear. It is known for other solution-processed ceramic thin films such as ceria or yttrium stabilized zirconia that the precursors and solvents can strongly impact the crystallization enthalpy, intermediate phases formed, and crystal growth rates.[30] Similar studies are lacking for the structurally more complex four-cation (LLZO) Li-garnet thin films. From an analytical perspective, it remains challenging to deconvolute this by classic structure determination techniques such as TEM and X-ray diffraction (XRD) due to the amorphous nature of the films after deposition, which is characterized by a complex interaction of undecomposed precursors, solvent residues and the already formed metal–oxygen network. Obtaining this knowledge, however, is important to understand the whole crystallization process of solution-processed LLZO films, potentially enabling tuneability of the process including crystallization temperature, control of grain sizes, mechanic properties, homogeneity, and phases formed through advanced precursor design.

In this study, we contribute to the in-depth understanding of ceramic precursor design and its impact on the forming ceramic for the example of an oxide based Li-ion solid electrolyte – Li-garnet (LLZO) – for next generation batteries. Specifically, we follow the phase evolutions and precursor decomposition events during annealing of solution-processed Li-garnet films, synthesized by spray-coating *via* Sequential Decomposition Synthesis (SDS). Unlike classic ceramic fabrication, where multi-steps with powder synthesis and densification are needed, SDS is a representative synthesis route for a direct liquid to solid translation resulting in dense battery-grade films of 1–10 μm. This makes it an attractive method for future scale-up at low production costs. During the annealing procedure, we identify several decomposition events of remaining solvent components and precursors occurring in parallel to the crystallization of the pyrochlore $La_2Zr_2O_7$ phase at a lower temperature, and of the cubic Li-garnet phase at higher temperatures. We elucidate changes in the local environment of the amorphous La–Zr–O network, deconvolute the contributions of each precursor salt to the occurring decomposition reactions and thereby reveal the importance of the high temperature decomposition of the Li-precursor $LiNO_3$ to the final LLZO phase formation. With this, we contribute to the understanding of the role of precursor design in the effective crystallization and phase formation of a solution-processed Li-oxide based ceramic film with a high number of cations (≥4).

Experimental

Preparation of LLZO films through SDS

The spraying solution was prepared by dissolving $Li(NO_3)$, $Al(NO_3)_3 \cdot 9H_2O$, $La(NO_3)_3 \cdot 6H_2O$, and Zr(IV)-acetylacetonate in a 1 : 1 : 1 mixture of methanol, 1-methoxy-2-propanol, bis(2-ethylhexyl)phthalate in the stoichiometric ratio of $Li_{6.25}Al_{0.25}La_3Z_2O_{12}$ (0.01 M) with an optimized lithium precursor excess of 76 mol%.[17] For spray pyrolysis, the precursor solution was pumped by a syringe pump through a spray head (DeVILBISS ag360) with a rate of 75 mL h^{-1}. Compressed air with a pressure of 0.3 bar served as carrier gas. The solution is sprayed on

a MgO (001) substrate at a surface temperature of 250 °C. After the deposition, the sample rested on the hotplate at the same temperature for 10 min. The as-deposited films were annealed in a box furnace (Carbolite Gero CWF 1100) applying a heating rate of 5 K min^{-1} to the specified annealing temperature which was held for 15 min before they cooled down to room temperature at uncontrolled natural cooling rate of the furnace. As reported previously, this method enables the fabrication of dense cubic LLZO films, which showed an ionic conductivity of 2.4×10^{-6} S cm^{-1} at 30 °C.[17]

Material characterization

Raman spectra were collected using a confocal alpha300 R Raman microscope (WITec) with a 532 nm excitation wavelength. The measurements were performed in air. All spectra were collected with a laser energy of 10 mW with an integration time of 5 s and averaged over 10 iterations.

The powder sample was packed in a 0.5 mm diameter borosilicate glass capillary and sealed with two-component epoxy in an argon-filled glovebox. High-resolution powder synchrotron X-ray diffraction (SXRD) patterns at the beam energy of 15 keV (wavelength = 0.824 Å) were acquired on beamline I11 at the Diamond Light Source, UK.

TGA and DSC measurements were performed on a TGA/DSC 3+ (Mettler Toledo) in MgO crucibles in an $O_2 : N_2$ 1 : 2 atmosphere. As-deposited films were fabricated without further annealing and the films were scratched off from the substrate to obtain a powder to fill into MgO crucibles. Measurements were performed with 5 K min^{-1} heating rate in the range of 25–750 °C while weight and heat flow were recorded simultaneously. The exhaust gases were directed into a ThermoStarTM GSD 320 gas analyzer (Pfeiffer Vacuum) to perform the mass spectrometry.

XPS measurements

For XPS measurements, all samples were mounted on a flag-style stainless steel sample holder equipped with a type K thermocouple to monitor sample temperature, with the thermocouple pressed against the top sample surface. To minimize exposure to ambient air, samples were stored in an argon-filled container prior to mounting onto the sample holders. After mounting, they were quickly transferred to the load-lock chamber and evacuated to vacuum. All samples were pumped in the load lock overnight (1×10^{-8} mbar pressure) to allow degassing of any residual volatile solvents.

The measurements were performed using a near-ambient pressure X-ray photoelectron spectroscopy setup (NAP-XPS, Specs Surface Nano Analysis GmbH) in a chamber with a base pressure of $<5 \times 10^{-9}$ mbar. An Al Kα X-ray source (power: 50 W, spot size: 120 μm) was used in most experiments, with some comparison spectra recorded with a Cr Kα source (power: 10 W, spot size: 200 μm). The analyzer was calibrated using sputter-cleaned copper (Cu), silver (Ag), and gold (Au) foils, with the Au $4f_{7/2}$, Ag $3d_{5/2}$, and Cu $2p_{3/2}$ core-level peaks positioned at 83.84, 368.11, and 932.50 eV, respectively.

All XPS spectra were acquired in fixed analyzer transmission (FAT) mode with a step size of 0.1 eV, a dwell time of 0.3 s, and a pass energy of 30 eV. High-resolution spectra for each core level were acquired with 10 scans in cyclic mode, meaning each scan for a given peak was collected after sequential scans of other peaks. This approach minimized the effect of temporal X-ray power fluctuations on the quantitative analysis. For films annealed at 300 and 400 °C, X-ray beam damage was observed; therefore, only the first scan was used for analysis.

The analysis chamber was backfilled with O_2 to a partial pressure of 10^{-6} mbar, with sample temperatures set to 100 °C for films annealed at 300 and 400 °C, and to 200 °C for those annealed at 500, 600, and 750 °C, to facilitate partial removal of surface carbonates. While the use of a lab-based X-ray source provides a stable excitation energy over the course of the experiment, binding energy calibration was still performed to account for sample charging effects. Due to the lack of stable internal reference points at higher annealing temperatures, a mixed referencing approach was employed: for the 300 and 400 °C samples, the presence of the C–C/C–H feature in C 1s allowed standard calibration to 284.8 eV.[34] At higher annealing temperatures, this adventitious carbon peak was absent due to decomposition, necessitating referencing based on the carbonate signals. The carbonate peak in the 750 °C annealed sample was at 290.1 eV in the C 1s spectrum and at 531.9 eV in O 1s matched literature values for Li_2CO_3.[35,36] Quantitative analysis also confirmed an atomic ratio of Li 1s : C 1s : O 1s close to 2 : 1 : 3, further supporting Li_2CO_3 assignment. Thus, for films annealed at 500, 600 and 750 °C, the carbonate C 1s peak at 290.1 eV served as the binding energy reference.

Curve fitting was performed using KolXPD[37] software. Spectra were fitted with one or several Gaussian–Lorentzian line-shape functions, and backgrounds were subtracted using a Shirley background. A constrained fitting approach was applied, where the peak full width at half maximum (FWHM) and binding energy positions were allowed to vary only slightly from initial estimates (±0.05 eV for FWHM and ±0.1 eV for binding energies).

Quantitative analysis was performed using the integrated area of fitted peaks, transmission-corrected for both analyzer and source transmission functions. The corrected integrated areas were then normalized by relative atomic sensitivity factors (RSFs), which for transmission-corrected spectra at the magic angle (54.7°) configuration—defined as the angle between the analyzer axis and X-ray source—are proportional to the product of the photoionization cross-section and inelastic mean free path (IMFP).[38] Photoionization cross-sections were determined using Scofield values,[39] while IMFP was calculated *via* the TPP-2M model provided by NIST.[40] However, owing to the inhomogeneous nature of film deposition and the surface sensitivity inherent to XPS, quantification of heavier elements such as Zr and La was less reliable. In contrast, quantification of Li and Li-related species proved more robust, permitting accurate identification of $LiNO_3$ and Li_2CO_3 phases within the samples. The quantitative results carry an estimated uncertainty of ±5% due to inherent limitations in this analytical approach.

Results and discussion

Structure evolution of as-deposited films during annealing

To follow the structure evolution of as-deposited Li-garnet during annealing, films were fabricated by the previously reported sequential decomposition synthesis (SDS) method,[17] (see Experimental section for more details), annealed at different temperatures and their structure was analyzed through Raman spectroscopy and synchrotron X-ray diffraction (SXRD). For the SDS fabrication, precursor salts (Li-, La, and Al-nitrates and Zr-acetylacetonate) were dissolved in a 1 : 1 : 1 mixture of methanol, 1-methoxy-2-propanol and bis(2-ethylhexyl)phthalate (DEHP) in stoichiometric amounts for the formation of $Li_{6.25}Al_{0.25}La_3Zr_2O_{12}$. For compensation of Li-loss, an excess of 76 mol% of the lithium precursor was used, as reported previously.[17] The solution was then sprayed on a single-crystalline MgO substrate at 250 °C surface temperature and the obtained films were annealed at different temperatures up to 750 °C. To confirm that no cation migration into the substrate took place during annealing, as it was observed for LLZO processed at >1000 °C,[15] ICP-OES measurements were performed before and after annealing at 750 °C (see Table S1, SI). Fig. 2a shows the Raman spectra of the as-deposited film and films after annealing to 400, 500, 600 and 750 °C and subsequent cooling to room temperature to obtain clear spectra and avoid thermal-induced noise. The as-deposited film and the film annealed at 400 °C show a very broad fluorescence signal in their Raman spectra, indicating organic residues from solvents of the spray process. The only peaks visible are those related to the Li-salt $LiNO_3$ at 249 and 1082 cm^{-1}, assigned to E_g and A_g Raman vibrational modes, respectively,[41] while signals from compounds with the remaining cations might remain shadowed by fluorescence due to a potentially amorphous nature and resulting broad Raman signals. When the temperature is increased to 500 °C, the background fluorescence signal disappears, indicating the decomposition of organic residues in the films. Instead, the $LiNO_3$ signal appears clearer with an additional peak visible at 737 cm^{-1}, the E_g Raman vibrational mode of $LiNO_3$, along with smaller signals stemming from the formation of Li_2CO_3. This is common for Li-garnets being exposed to moisture and CO_2 from the atmosphere, indicating that at this temperature, $LiNO_3$ is already starting to decompose to make lithium cations available for water and CO_2 uptake to form Li_2CO_3.[42,43] When the temperature is further increased to 600 °C, $LiNO_3$ signals have disappeared, proving the complete decomposition of this precursor salt, and the appearance of a broad peak at 306 cm^{-1} indicates the formation of LZO, which is usually observed in solution-based LLZO synthesis as an

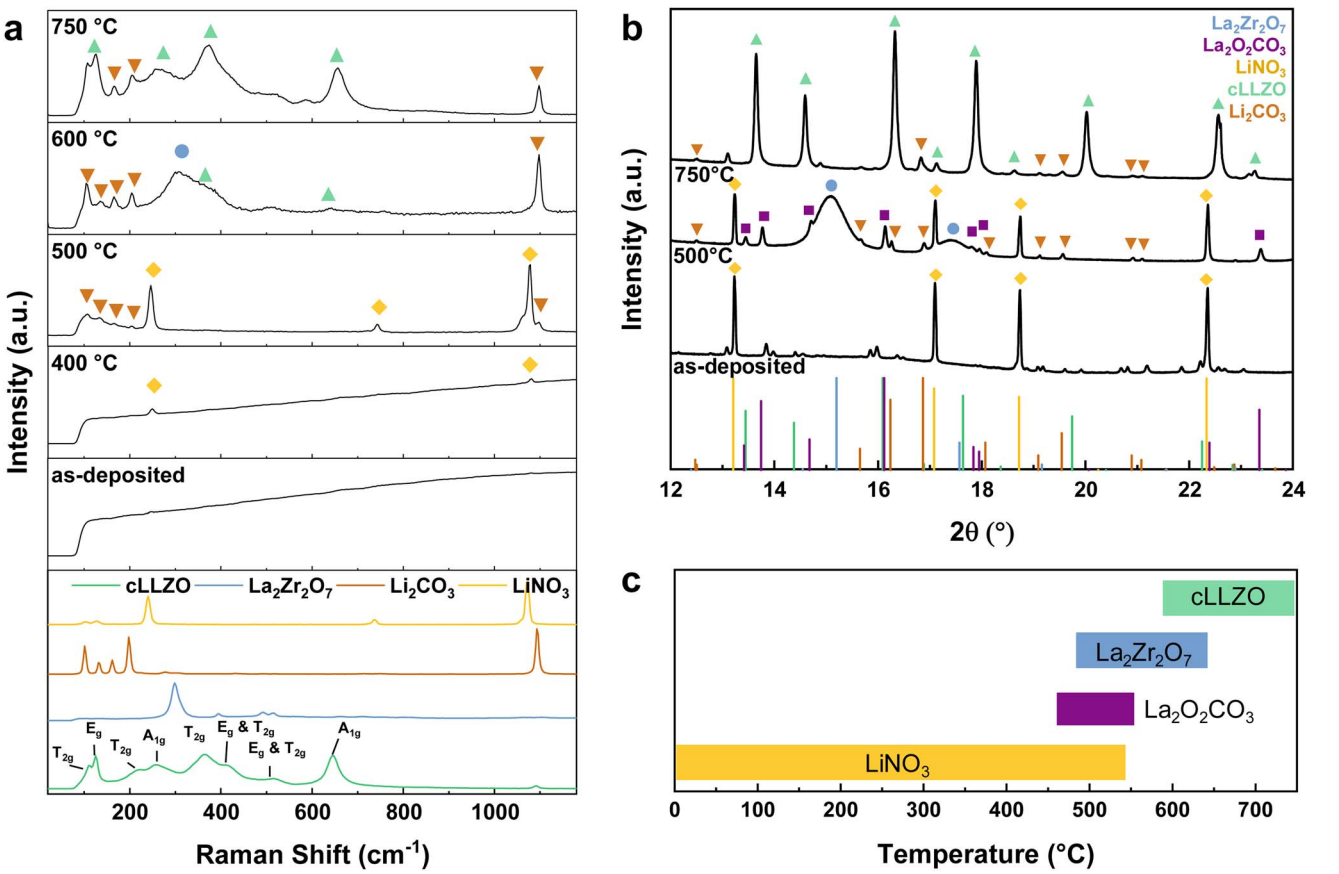

Fig. 2 (a) Raman spectra and (b) synchrotron X-ray diffractograms (wavelength = 0.8243 Å) of as-deposited and *ex situ* annealed Li-garnet films after cooling to room temperature. References of $LiNO_3$ (yellow), Li_2CO_3 (orange), LaO_2CO_3 (purple), $La_2Zr_2O_7$ (blue) and cubic LLZO (green). (c) Overview of phase evolutions with increasing annealing temperature as determined by Raman spectroscopy and SXRD.

intermediate which transforms to LLZO upon lithiation at higher temperatures.[21] This process is already initiated at 600 °C and is completed at 750 °C when the Raman spectrum shows characteristic peaks of the cubic LLZO phase. Aluminum doped cubic LLZO shows several characteristic peaks in Raman spectroscopy at 107, 121, 209, 251, 361, 410, 514, and 645 cm^{-1} attributed to T_{2g}, E_g, T_{2g}, A_{1g}, T_{2g}, E_g and T_{2g}, T_{2g} and E_g, and A_{1g}, Raman vibrational modes, respectively.[44,45] To validate the structural information obtained from Raman spectroscopy, SXRD measurements were performed for selected films in as-deposited state and after annealing at 500 and 750 °C (Fig. 2b). They reveal that nucleation of LZO from the amorphous phase already starts at 500 °C, showcased by broad reflexes at the LZO positions. This is in accordance with the temperature observed in other studies for LZO nucleation and crystallization, with the resulting nuclei being potentially too small to contribute to the Raman spectrum.[21] In addition, reflections of hexagonal $La_2O_2CO_3$ (COD-1000463) are visible at the same temperature, a common product that forms upon reaction of lanthanum oxide phases with moisture and CO_2 from the atmosphere.[43,46]

In summary, structural analysis provides an initial insight into phase transitions and precursor decomposition during the annealing of as-deposited LLZO films (Fig. 2c). It reveals that $LiNO_3$ salt remains undecomposed until temperatures beyond 500 °C. This finding is in contrast to previous studies, which observed $LiNO_3$ decomposition already between 400 and 500 °C and the observation of a fully amorphous film at 500 °C in *in situ* HR-TEM.[21] A possible explanations for this deviation is that $LiNO_3$ melts at 250 °C, which makes it difficult to observe in TEM and the decreased decomposition temperature in vacuum compared to ambient pressures usually applied during annealing of ceramic films. Beyond this, it remains unclear from the SXRD and Raman data, to which extent the precursors of lanthanum and zirconium are already decomposed in the as-deposited film and which lanthanum and zirconium phases are involved in the formation of crystalline LZO and later LLZO cannot be resolved due to their amorphous nature and fluorescence shadowing. To elucidate this, in-depth thermal analysis was performed to follow decomposition events and phase changes in the material during the annealing process.

Characterization of precursor decomposition and phase changes

To follow the decompositions and phase changes during heating, the as-deposited films were investigated through simultaneous thermal analysis (STA), which combines thermogravimetric analysis (TGA) and differential scanning calorimetry (DSC). This allows to determine weight changes through TGA while simultaneously following decomposition reactions of precursors or phase changes in the material through DSC. In addition, a mass spectrometer connected to the exhaust reveals the nature of evolving gases with respect to the sample temperature.

When heating the as-deposited Li-garnet from room temperature to 750 °C in O_2 : N_2 1 : 2 atmosphere, six events (**1–6**) are visible in STA (Fig. 3a and Table S2, SI). *Via* mass spectrometry (MS) the nature of these events can be resolved by identifying the exhausted gases. Fig. 3b shows the mass spectrometry signals from the most important fragments involved in the reactions taking place in the material during annealing. Water evolution can be detected at a mass over charge ratio of *m*/*z* 18 stemming from H_2O^+, the most important fragment of water in MS. When nitrates decompose, several fragments of nitrogen oxides are formed: *m*/*z* 30 (NO^+), 44 (N_2O^+), 46 (NO_2^+) and 47 (HNO_2^+) along with 36 (O_2^+). As oxygen is also part of the analysis gas, any changes in concentration are easily diluted, which is why this signal was not further investigated.

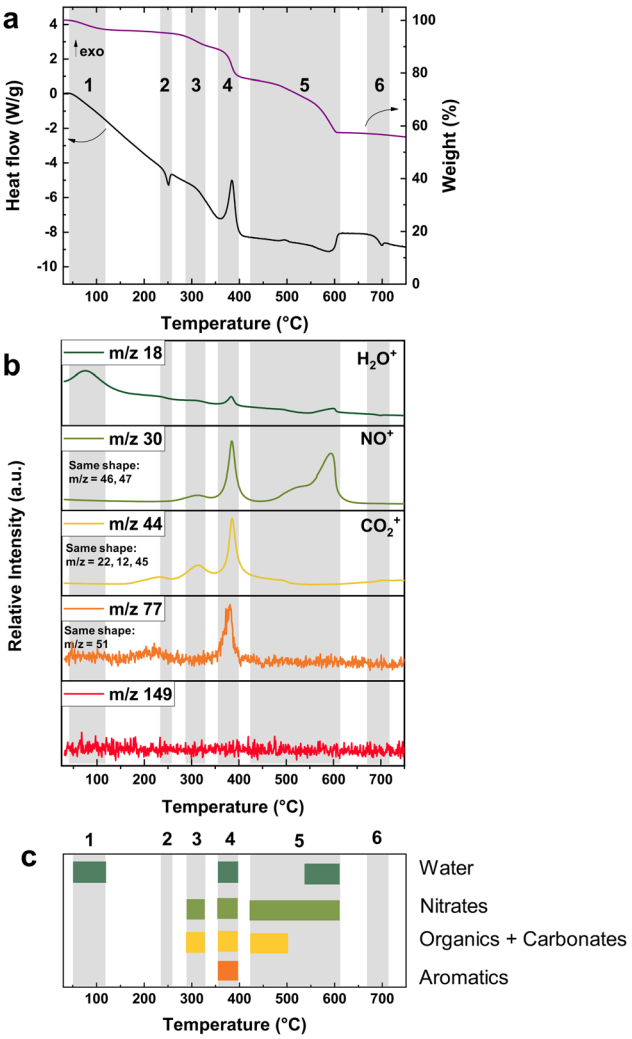

Fig. 3 (a) TGA/DSC curves of as deposited Li-garnet and (b) mass spectrometry of evolving gases recorded during heating to 750 °C. Traces of the main MS fragments with a mass over charge ratio of *m*/*z* 18, 30, 44, 77 and 149 are shown exemplarily for evaporation of water, decomposition of nitrates, organics and carbonates, aromatics, and DEHP, respectively. Related fragments of the decomposition of nitrates (*m*/*z* 46, 47), organics and carbonates (*m*/*z* 12, 22, and 45) and DEHP (*m*/*z* 51) are not shown separately but help confirm the assignments made due to same shapes of the recorded traces. (c) Summary of evaporating or decomposing compounds with respect to the temperature applied.

Additionally, care has to be applied with the fragment m/z 44, which is not only visible as a minor fragment in the decomposition of nitrates, but also, more prominently, the main fragment of carbon dioxide (CO_2^+) involved in the decomposition of many organic materials. Important fragments related to the decomposition of organics in oxidizing atmosphere are m/z 12 (C^+), 22 (CO_2^{2+}), 28 (CO^+), 44 (CO_2^+) and 45 (HCO_2^+). In addition to these expected fragments, the fragments m/z 51 and 77 appeared, exclusively simultaneously, which can be related to common MS fragments from decomposing aromatic components such as phthalate esters.[47]

In the temperature range from room temperature to 175 °C (**1**), water evaporates from the sample resulting in a total weight loss of 4.1%. This can be confirmed through MS which shows a peak only for m/z 18. Water is easily adsorbed on the surface of as-deposited Li-garnet films due to the hygroscopicity of the undecomposed nitrate precursors. The second and third event partially overlap in the same temperature range: a phase transition discernable from the endothermic peak in the heat flow which is not related to a weight loss at 230–260 °C (**2**) and a broad exothermic event related to a weight loss of 6.5% at 175–350 °C (**3**). The former can be attributed to melting of $LiNO_3$ at 250 °C,[48] the presence of which in the as-deposited film was already confirmed by Raman spectroscopy and SXRD. The latter is a decomposition resulting in carbon dioxide and minor nitrogen oxide release indicating the decomposition of carbonaceous compounds and nitrates at the same time. More specifically, the carbon dioxide formation could either result from decomposition of solvent residues in the material, acetylacetonate ligands from the zirconium precursor, or other metal carbonates formed in the material during deposition. This is followed by a more prominent exothermic event along with a weight loss of 12.4% at 350–445 °C (**4**). The previously observed nitrogen oxide and carbon dioxide signals reappear at higher intensities along with fragments with m/z 51 and 77. As discussed before, these appear together usually in decomposition reactions of aromatic compounds, indicating that residues from the high-temperature boiling point solvent DEHP, which is the only aromatic compound used in this system, are remaining in the as-deposited film up to an annealing temperature of 445 °C. Interestingly, no signal is observed for m/z 149, which is the most prominent fragment in the decomposition of DEHP. This suggests that the DEHP is already partially decomposing during the deposition of the Li-garnet film, resulting in aromatic residues that differ in their thermal decomposition from DEHP. However, not only the aromatic solvent residues are decomposing in this event, but also the first of two prominent nitrate decompositions is observed. The second prominent nitrate decomposition appears at 445–650 °C. This endothermic two-step event (**5**) results in the biggest weight loss of 19.7% and except of nitrates and traces of water, no other decomposition products are observed in MS. Finally, an endothermic phase transformation is observed in the temperature range of 650–750 °C (**6**), which aligns well with the reported temperature range of tetragonal to cubic LLZO transformation.[43]

In summary, simultaneous thermal analysis coupled with mass spectroscopy reveals that in the as-deposited Li-garnet first water, then mostly organics and finally nitrates decompose (Fig. 3c): solvents and potentially organic ligands from precursors remain in the as-deposited films and are fully decomposed for temperatures exceeding 400 °C. Nitrates decompose in two major steps, at 350–445 °C and at 445–650 °C. From SXRD and Raman spectroscopy, it is confirmed that $LiNO_3$ decomposes between 500 and 600 °C indicating that the second nitrate decomposition visible in STA stems from decomposition of $LiNO_3$. This can be confirmed when calculating the reaction enthalpy based on the weight loss from TGA, the integrated heat flow from DSC and the reaction equation of $LiNO_3$ decomposition:

$$LiNO_3 \rightarrow 0.5Li_2O + 0.25O_2 + NO_2,\ \Delta_r H^\circ = 217.6\ \text{kJ mol}^{-1}$$

If all weight losses observed in the temperature range from 445 to 650 °C result from a 1 : 4 molar ratio of O_2 to NO_2, then the measured heat flow results in a reaction enthalpy of 226 kJmol^{-1}. Even though a limited accuracy is anticipated due to the small amounts of water observed in the mass spectrometer which are not considered in the calculation, this is very close to the calculated standard reaction enthalpy of $\Delta_r H^\circ = 217.6$ kJ mol^{-1}. It remains unclear, however, whether the lithium nitrate decomposes here in two steps, or whether the first nitrate decomposition step at 350–445 °C results from another nitrate species present in the as-deposited films.

To confirm the assignments made and to further deconvolute the precursor nitrate decompositions, films with varying combinations of the four precursors salts of Li, La, Zr, and Al were fabricated and analyzed in STA (Fig. 4, S1–S3 and Tables S2–S8, SI). By step by step reducing the number of cations involved, the role of different cations in the phase evolution of the as-deposited Li-garnet can be evaluated. An overview of the compositions investigated can be seen in Fig. 4a.

When the aluminum salt is removed from the precursor solutions, *i.e.* only lithium, lanthanum and zirconium precursors remain ("Li–La–Zr-mix"), the STA data (Fig. 4b and c) is almost identical to the full Li-garnet ("Al–Li–La–Zr-mix") except of event (**6**), previously assigned to the tetragonal to cubic LLZO transition, which does not exist in the Li–La–Zr-mix sample because of the missing Al-dopant to stabilize the cubic phase.

Comparing the films fabricated from precursor solutions of La only, Zr only, Al only and La–Zr-mixture, it becomes evident that the exothermal event (**4**) related to the decomposition of aromatics and potentially other organic residues (see fragments m/z 44 and 77) are shifted to higher temperatures compared to the as-deposited Li-garnet material. The peak position of the heat flow is at 388 °C for the Al : LLZO and is shifted to 444 °C (La–Zr-mix), 462 °C (Zr-only), 497 °C (La-only) and 499 °C (Al-only) indicating that the organic solvent residues are bound differently strongly to the material structure, depending on the amount and type of cations involved in the materials. Interestingly, the film fabricated only from the lithium precursor solution (Li-only), does not release any organic decomposition

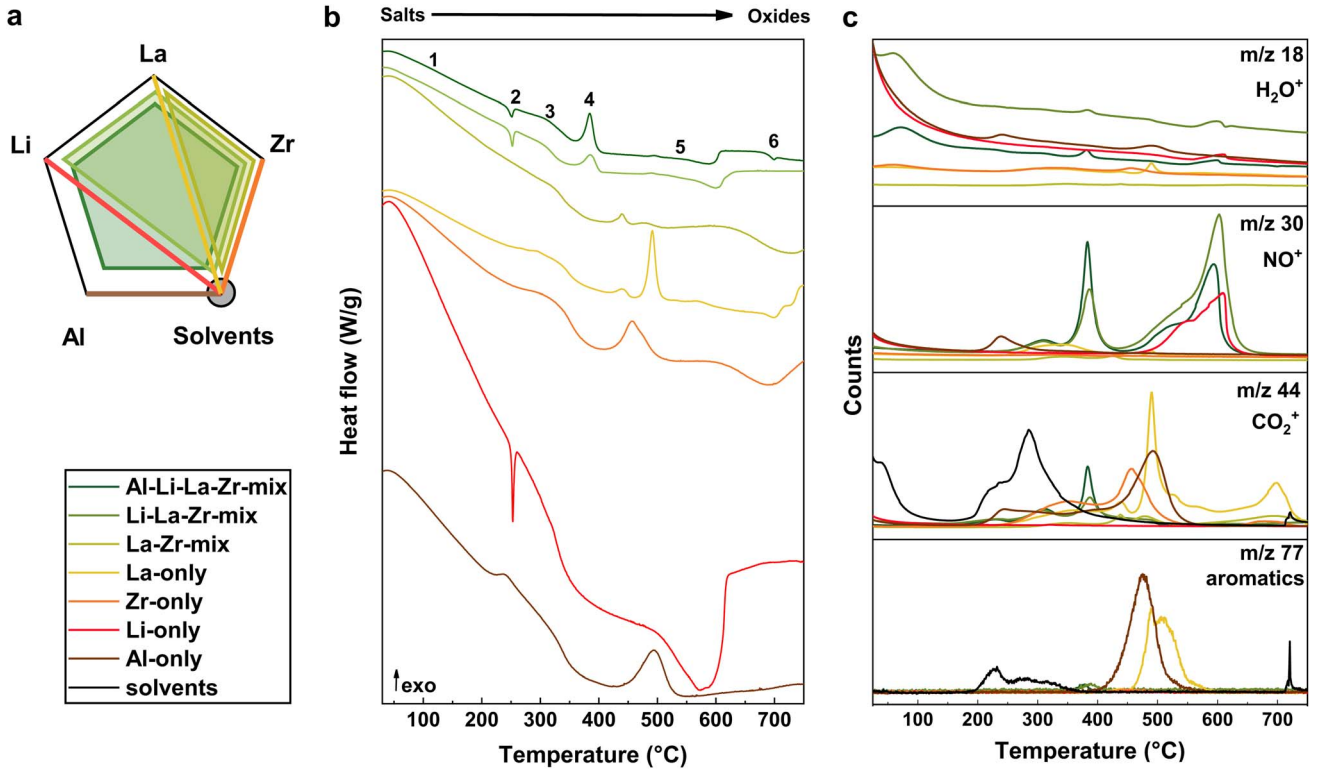

Fig. 4 (a) Schematic representation of the combinations of precursor salts used to fabricate films: Li, Al, La, and Zr (dark green), Li, La, and Zr (light green), La and Zr (dark yellow), La (yellow), Zr (orange), Li (red), Al (brown) and pure solvents (black). DSC curves (b) and mass spectrometry of evolving gases (c) of all combinations during heating to 750 °C in STA.

products, even though the same solvents are used in its preparation. This might be explained by the fact that the Li-only film is in a liquid state during deposition due to the molten and undecomposed $LiNO_3$ precursor and therefore doesn't incorporate any organics from the solvents. This can also be observed by eye, when the Li-only film crystallizes upon removal from the spray chamber.

Considering the nitrate decomposition signals (m/z 30), none of the non-Li-containing films releases a large amount of nitrogen oxides that could explain the origin of the first large nitrate decomposition event (**3**) of as-deposited Al : LLZO. Also in the Li-only film, this event is not visible, even though the second big nitrate decomposition event (**4**) is very well covered by the Li-only mass spectrum and heat flow further proving the $LiNO_3$ decomposition at this temperature. However, in all films that contain a nitrate precursor salt, the strongly exothermic decomposition of aromatic solvent residues is connected to a nitrogen oxide release. This suggests that the large amount of heat that is locally generated during the decomposition of the organic material is driving the endothermic nitrate decomposition at lower temperatures than usual, as it is described in literature for other solution-processed oxide thin film materials.[19]

These results suggest that the two-step nitrate decomposition in as-deposited Al : LLZO upon heating stems from two separate $LiNO_3$ decomposition steps: the first one at 350–445 °C (**4**) triggered by the exothermic decomposition of aromatic solvent residues and the second one at 445–650 °C (**5**) being the conventional $LiNO_3$ decomposition as also observed in the Li-only film. This can be supported by the overall expected weight loss related to the Li-precursor salt decomposition. The LLZO material after heating the as-deposited Li-garnet to 750 °C accounts for a residual weight of 56% with respect to the as-deposited starting material. Meanwhile, the expected weight loss resulting from the $LiNO_3$ decomposition is around 30%, depending on the exact stoichiometry of the LLZO material after heating. Events **4** and **5**, which besides nitrate decomposition also include organics decomposing, show a weight loss of 12.4% and 19.7%, respectively, matching the expected 30% weight loss due to $LiNO_3$ decomposition (see Table S2, SI). The other metal cations, however, only contribute small amounts of remaining precursors that decompose during the heating, which proves that they already form an amorphous metal–oxygen network during the deposition. What cannot be resolved in this analysis is the crystallization enthalpy of LZO and tetragonal LLZO, being shadowed by the strong heat flows related to decomposition reactions. This is, again, in contrast to previous studies, where the enthalpy of event **5** was attributed exclusively to the LLZO crystallization enthalpy while $LiNO_3$ decomposition was assigned to event **4** due to the previously discussed assignment of $LiNO_3$ decomposition to lower temperatures.[31]

Evolution of local chemical environment during annealing

X-ray photoelectron spectroscopy (XPS) was performed on *ex situ* annealed Li-garnet films to monitor chemical changes in

the local cation environment during annealing (Fig. 5, S4 and Table S9, SI). To mitigate charging effects associated with the insulating nature of the ceramic films on MgO substrates, all XPS measurements were conducted at elevated temperatures under an oxygen atmosphere.[49] Exposing the samples to O_2 during XPS measurements will have negligible effects on chemical states of the samples as they were pre-annealed in air atmosphere. Overall, negligible charging was observed for all samples except the 600 °C film, which exhibited a +0.3 eV shift relative to Li_2CO_3. For more details on charge correction and measurement conditions see Experimental section.

High resolution XPS spectra of C 1s, N 1s, O 1s, Li 1s, Zr 3d, and La $3d_{5/2}$ core levels of films annealed at temperatures ranging from 300 to 750 °C are shown in Fig. 5a–f, respectively. In the range 300–500 °C, fitted peaks (see Experimental section for information on peak fitting) at 407.2–407.8 eV (N 1s), 532.8–533.5 eV (O 1s), and 56.1–56.7 eV (Li 1s) confirm the presence of $LiNO_3$. Also, the ratio of peak intensities calculated using relative atomic sensitivity factors (see Experimental section) for Li 1s : N 1s : O 1s, obtained from quantitative analysis of the XPS data (see Table S10, SI), is close to 1 : 1 : 3, supporting the assignment of $LiNO_3$ in the range of 300–500 °C. Interestingly, the N 1s peak shifts to higher binding energies as the annealing temperature increases from 300 to 500 °C, suggesting changes in the environment around $LiNO_3$. This is consistent with the decomposition of other precursors, as discussed later in this

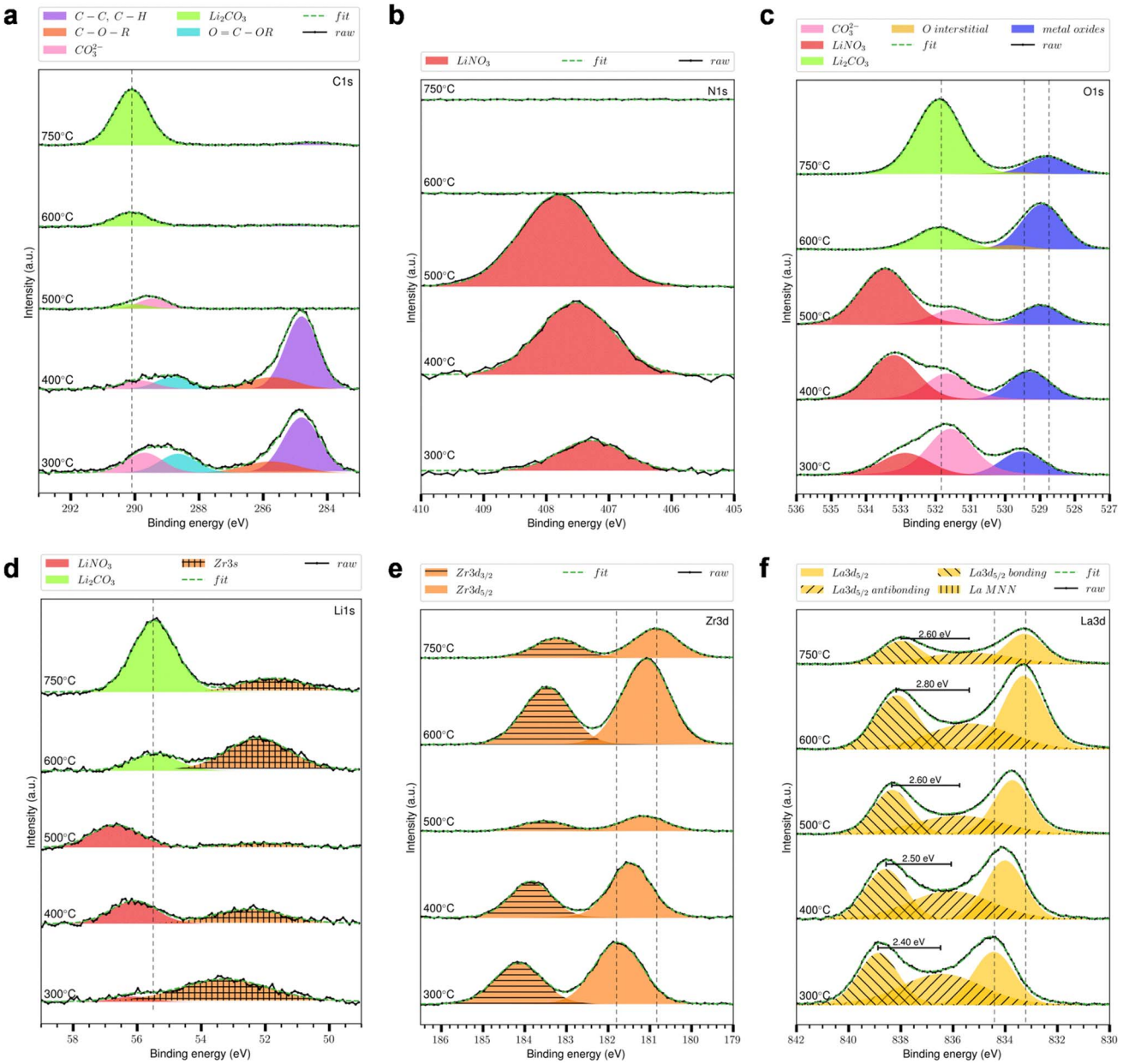

Fig. 5 XPS detail spectra showing the phase evolution of LLZO films *ex situ* annealed from 300 to 750 °C for contributions of (a) C 1s, (b) N 1s, (c) O 1s, (d) Li 1s, (e) Zr 3d, (f) La $3d_{5/2}$.

section and earlier in the Raman and XRD analyses. A similar shift is observed in the Li 1s peak, confirming that the changes arise from modifications to the $LiNO_3$ environment rather than the formation of other metal nitrates.

At 600 °C and 750 °C, peaks at 531.9 eV (O 1s), 290.1 eV (C 1s), and 55.4 eV (Li 1s), combined with the absence of an N 1s signal, confirm complete decomposition of $LiNO_3$ and formation of Li_2CO_3 on the surface, supported by an intensity ratio of Li 1s : C 1s : O 1s which is close to 2 : 1 : 3. Attempts to remove Li_2CO_3 on 750 °C annealed sample as reported[50] by annealing first in ultra-high vacuum (UHV) and then in 10^{-6} mbar O_2 at 350 °C for 30 min each were unsuccessful as shown in Fig. S5 (SI), indicating that the carbonate layer was too thick for complete removal at these conditions. Annealing at even higher temperatures, as reported elsewhere,[51,52] was not beneficial due to an observed lithium loss and LLZO degradation. The LLZO contribution to Li 1 s in 600 and 750 °C annealed samples could not be resolved due to the Li_2CO_3 layer on the surface and the similarity of their binding energies.[42]

Multi-component C 1s spectra were observed for the 300 and 400 °C samples, with components corresponding to aromatic/aliphatic C–C and C–H (284.8 eV), esters/alcohols (285.7 eV), and esters/carboxyls (288.6–288.8 eV), indicating residual solvents or acetylacetonate ligands in films at lower annealing temperatures.

The binding energies of zirconium (Zr 3d), lanthanum (La $3d_{5/2}$), and metal oxide (O 1s) show a decreasing trend with increasing annealing temperature. Zr $3d_{5/2}$ binding energies were 181.8 eV (300 °C), 181.5 eV (400 °C), 181.2 eV (500 °C), 181.1 eV (600 °C), and 180.9 eV (750 °C). This matches literature values, where higher binding energies (181.4–181.9 eV) are reported for LZO[53,54] compared to 180.8–180.1 eV for LLZO.[42,55,56] These results confirm the decomposition of zirconium acetylacetonate during deposition and the formation of an amorphous La–Zr–O network, as the precursor binding energy (182.3 eV)[57] is significantly higher. A similar trend is observed for La $3d_{5/2}$, with binding energies of 834.4 eV (300 °C), 834.0 eV (400 °C), 833.7 eV (500 °C), and 833.3 eV (600 °C and 750 °C). As with zirconium, the decreasing trend supports the gradual transformation of LZO into LLZO, in agreement with literature binding energies of 834.6–834.9 eV (ref. 53 and 54) and 833.2–833.7 eV,[55,56] respectively. Interestingly, Zr $3d_{5/2}$ stabilizes at 500 °C, while La $3d_{5/2}$ continues to shift until 600 °C, possibly due to more significant structural rearrangements affecting La local bonding compared to the more rigid Zr network.[21]

An additional observation from the La 3d spectra concerns the variation in energy separation between the bonding and antibonding satellite peaks, which serves as an indicator of the degree of hybridization between La 4f orbitals and the ligands' valence band.[58] These satellite features arise from charge transfer processes involving ligand atoms and core-ionized La 4f states. While full spectral fitting of La 3d is complicated by significant multiplet splitting, the La $3d_{5/2}$ region was analyzed using one principal peak with two satellites (bonding and antibonding), adopting fitting parameters reported by Sunding *et al.*[59] As shown in Fig. 5f, the bonding–antibonding separation increases from 2.4 eV to 2.8 eV as the annealing temperature is raised from 300 °C to 600 °C, signifying increased hybridization and enhanced La–O covalency within the oxide structures. Upon annealing at 750 °C, this separation decreases to 2.6 eV, suggesting a further modification in La–O hybridization. (See Fig. S6, SI for a more detailed discussion.)

Collectively, these measurements agree well with the previous structure and thermal analysis results confirming the observed trends of organics and lithium nitrate decompositions at below 500 °C and below 600 °C, respectively. Furthermore, they show the gradual transformation of the amorphous La–Zr–O network with partially undecomposed precursors into crystalline LLZO from as-deposited state until a temperature of 750 °C is reached and the final cubic LLZO phase is formed.

Decompositions and phase changes involved in the crystallization of solution-processed cubic Li-garnet films

In the following, we summarize the sequence of precursor decompositions and phase changes leading to the formation of the crystalline cubic phase of LLZO from a solution-processed as-deposited ceramic film (Fig. 6). To understand the role of initial metal salts and respective cations in the formation of the multi-cation ceramic compound, we performed structural and thermal analysis, together with X-ray photoelectron spectroscopy as evidence for the discussion.

Solvent and precursor decomposition reactions. During annealing of the as-deposited ceramic film, several precursor and solvent decompositions are identified. At lower temperatures, remaining organic residues decompose in two major steps in the temperature range of 270 to 400 °C. During the first step, mostly carbon dioxide is emitted suggesting the decomposition of smaller solvent or precursor ligand molecules. In the second, more strongly exothermic organic decomposition step, aromatic fragments are observed in addition to the prominent carbon dioxide peak, proving the decomposition of residues of the high-temperature boiling point solvent DEHP remaining in the ceramic film after the deposition. At higher temperatures, nitrate precursors, remaining in the film after deposition, decompose. This reaction proceeds in two major steps as evidenced by the release of nitrogen oxide gas: the first step occurs in parallel to the aromatic solvent decomposition, while a second decomposition is observed at 450 to 600 °C.

The role of individual precursors on the decomposition events. Investigating films with varying combinations of the four precursor salts helps to deconvolute the contribution of the individual precursor salts to these decomposition events. The aluminum, lanthanum and zirconium precursors are mostly decomposed already during the deposition and only add small amounts of organic and nitrogen oxide emissions below 400 °C. The lithium precursor, $LiNO_3$, is more stable and is the only precursor that contributes significantly to the nitrogen oxide release, being responsible for the two major nitrogen oxide emission events. The first of them, observed in parallel to the aromatic solvent decomposition, stems from an early partial decomposition of $LiNO_3$ due to the strong exothermic reaction of the decomposing solvent.

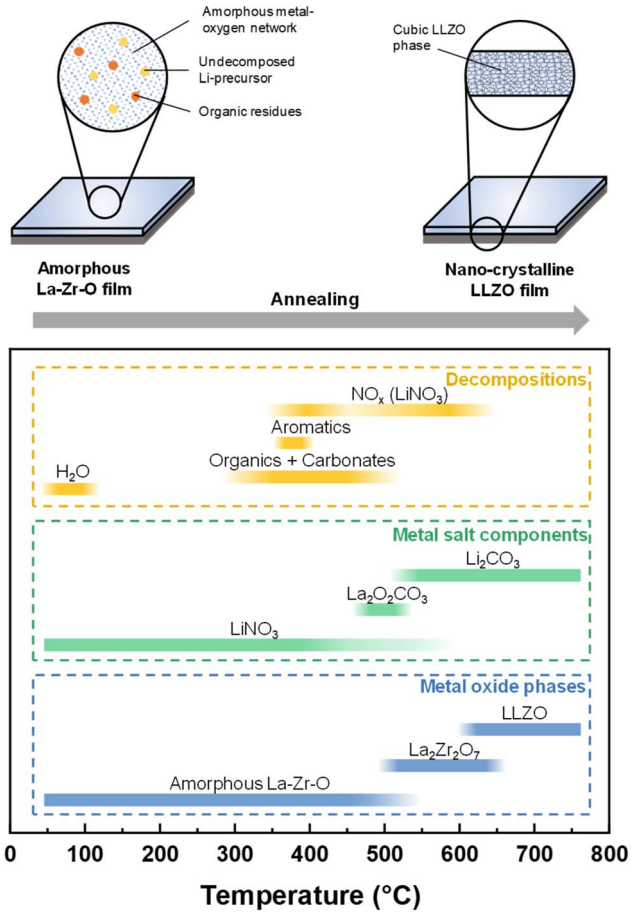

Fig. 6 Schematic summary of the structure evolution from as-deposited to crystalline cubic Li-garnet material derived from a solution-based ceramic synthesis. Identified metal salts, metal oxide phases and decomposition reactions involved in the formation of crystalline cubic LLZO from solution-processed films are shown with respect to the annealing temperature.

Crystallization and phase formation. During the deposition, the ceramic film forms as an amorphous La–Zr–O network with the previously discussed undecomposed precursor and solvent residues. At around 500 °C, nuclei of pyrochlore $La_2Zr_2O_7$ (LZO) form from the amorphous La–Zr–O network, consistent with earlier observations on solution-processed LLZO films.[20,25,26] In parallel with the LZO nucleation, we observe the decomposition of the lithium precursor, $LiNO_3$, a requirement for the formation of the crystalline LLZO phase; this phase forms, as observed in previous TEM studies, through lithium diffusion into the LZO nuclei from the amorphous surroundings.[21]

This knowledge significantly helps to understand the processes involved in the crystallization of solution-processed ceramic films showing the impact of precursor decompositions on the phases formed at different temperatures. In the future, based on this, advanced precursor design could help to gain better control over crystallization temperatures, grain sizes, film homogeneity and phases formed. For example, reducing the decomposition temperature of the Li precursor used to fabricate LLZO films could improve the availability of lithium ions for ceramic structure formation at lower temperatures. To confirm this, future work could explore precursor classes with different decomposition temperatures and study their impact on the crystallization process of the ceramic material to provide greater flexibility in processing methods and temperatures, improve integration with other battery components, and enhance the sustainability of next-generation battery materials.

Conclusions

In ceramic synthesis, designing precursors for solution-based film fabrication remains a challenge, as the initial precursor solubility, reactivity, and decomposition impact the required annealing protocol, film microstructure, and phases formed at the same time. Even though solution-based film fabrication of oxide ceramics is an established technique for a variety of materials, less attention is drawn to the impact of precursor design on the crystallization process. However, this understanding is important as the structure of materials gets more complicated along with an increasing number of cations to control during phase formation. To study this, we selected Li-garnet, an oxide-based lithium-ion solid electrolyte for next generation batteries, as a model material. Li-garnet is a good representative of a ceramic material with a high number of cations and dopants to control in the precursor design and phase evolution, while being a technologically relevant material class to provide cost-reduced ceramic manufacture.

This study provides a comprehensive investigation of the structure evolution, precursor decompositions and phase transformations occurring during the annealing of solution-processed $Li_{6.25}Al_{0.25}La_3Zr_2O_{12}$ (LLZO) films. By combining classic structure analysis techniques such as SXRD and Raman spectroscopy with thermal analysis and XPS, we can elucidate the transformation of the as-deposited amorphous La–Zr–O network into crystalline cubic LLZO. The impact of each individual precursor salt, namely $Li(NO_3)$, $Al(NO_3)_3 \cdot 9H_2O$, $La(NO_3)_3 \cdot 6H_2O$, and Zr(IV)-acetylacetonate, on the observed decomposition events was identified by investigating different combinations of precursors used for the fabrication of as-deposited ceramic films. From this, it can be concluded that aluminum, lanthanum and zirconium precursors are already mostly decomposed after the deposition at 250 °C to form an amorphous metal–oxygen network, while the lithium precursor, $LiNO_3$, remains crystalline and undecomposed at this stage. Upon annealing, $LiNO_3$ decomposes in two steps enabling the incorporation of lithium into the in parallel crystallizing $La_2Zr_2O_7$ (LZO) phase forming the cubic LLZO phase.

This coupling of precursor decomposition and crystallization suggests that the nature of the precursors and solvents has a significant impact on the crystallization process of solution-processed ceramic LLZO films. Based on this, the tuneability of the crystallization process of LLZO utilizing different precursor chemistries is to be explored in future work. Collectively we contribute through the work to the understanding of precursor design principles for cost-effective direct liquid-precursor-to-solid-film manufacturing routes of solid-state battery electrolyte ceramics.

Author contributions

L. Q. and J. L. M. R. conceived the idea of this study, designed the experiments and discussed the data and interpretation. G. A. performed and analyzed the XPS measurements. F. N. S. performed the SXRD measurements. L. Q. performed all other experiments and wrote the manuscript. All co-authors provided feedback and expertise on data analysis and manuscript.

Conflicts of interest

The authors declare no competing interests.

Data availability

The data supporting this article have been included as part of the supplementary information (SI). Further datasets are available upon request from the corresponding author. Supplementary information is available. See DOI: https://doi.org/10.1039/d6ta02188c.

Acknowledgements

This work was funded by the Deutsche Forschungsgemeinschaft (DFG, German Research Foundation) under Germany's Excellence Strategy EXC 2089/1-390776260. F. N. S. and C. P. G. acknowledge funding from the Faraday Institution CATMAT (FIRG016) and Degradation (FIRG082) projects. The authors acknowledge the I11 beamline at the Diamond Light Source, UK, for the SXRD measurement done under "Cambridge BAG for new materials characterization and structure–property relationships for a zero-carbon future" (CY34243).

References

1 M. M. Raju, F. Altayran, M. Johnson, D. Wang and Q. Zhang, Crystal Structure and Preparation of $Li_7La_3Zr_2O_{12}$ (LLZO) Solid-State Electrolyte and Doping Impacts on the Conductivity: An Overview, *Electrochem*, 2021, **2**, 390–414.

2 C. Wang, K. Fu, S. P. Kammampata, D. W. McOwen, A. J. Samson, L. Zhang, G. T. Hitz, A. M. Nolan, E. D. Wachsman and Y. Mo, Garnet-type solid-state electrolytes: materials, interfaces, and batteries, *Chem. Rev.*, 2020, **120**, 4257–4300.

3 A. J. Samson, K. Hofstetter, S. Bag and V. Thangadurai, A bird's-eye view of Li-stuffed garnet-type $Li_7La_3Zr_2O_{12}$ ceramic electrolytes for advanced all-solid-state Li batteries, *Energy Environ. Sci.*, 2019, **12**, 2957–2975.

4 M. Balaish, J. C. Gonzalez-Rosillo, K. J. Kim, Y. Zhu, Z. D. Hood and J. L. Rupp, Processing thin but robust electrolytes for solid-state batteries, *Nat. Energy*, 2021, **6**, 227–239.

5 S. Randau, D. A. Weber, O. Kötz, R. Koerver, P. Braun, A. Weber, E. Ivers-Tiffée, T. Adermann, J. Kulisch, W. G. Zeier, F. H. Richter and J. Janek, Benchmarking the performance of all-solid-state lithium batteries, *Nat. Energy*, 2020, **5**, 259–270.

6 K. J. Kim, M. Balaish, M. Wadaguchi, L. Kong and J. L. Rupp, Solid-state Li–metal batteries: challenges and horizons of oxide and sulfide solid electrolytes and their interfaces, *Adv. Energy Mater.*, 2021, **11**, 2002689.

7 M. Balaish, K. J. Kim, H. Chu, Y. Zhu, J. C. Gonzalez-Rosillo, L. Kong, H. Paik, S. Weinmann, Z. D. Hood, J. Hinricher, L. J. Miara and J. L. M. Rupp, Emerging processing guidelines for solid electrolytes in the era of oxide-based solid-state batteries, *Chem. Soc. Rev.*, 2025, **54**, 8925–9007.

8 H. Sun, S. Kang and L. Cui, Prospects of LLZO type solid electrolyte: from material design to battery application, *Chem. Eng. J.*, 2023, **454**, 140375.

9 P. Badami, S. Smetaczek, A. Limbeck, D. Rettenwander, C. K. Chan and A. N. M. Kannan, Facile synthesis of Al-stabilized lithium garnets by a solution-combustion technique for all solid-state batteries, *Mater. Adv.*, 2021, **2**, 5181–5188.

10 K. Ghosh and M. Wasim Raja, Engineered $Li_7La_3Zr_2O_{12}$ (LLZO) for Pseudo-Solid-State Lithium Metal Batteries (SSLMBs): Tailor-Made Synthesis, Evolution of the Microstructure, Suppression of Dendritic Growth, and Enhanced Electrochemical Performance, *ACS Appl. Energy Mater.*, 2023, **6**, 4035–4052.

11 J. Sakamoto, E. Rangasamy, H. Kim, Y. Kim and J. Wolfenstine, Synthesis of nano-scale fast ion conducting cubic $Li_7La_3Zr_2O_{12}$, *Nanotechnology*, 2013, **24**, 424005.

12 R. A. Jonson, E. Yi, F. Shen and M. C. Tucker, Optimization of Tape Casting for Fabrication of $Li_{6.25}Al_{0.25}La_3Zr_2O_{12}$ Sheets, *Energy Fuels*, 2021, **35**, 8982–8990.

13 H. Pan, L. Fan, Y. Zhang, L. Zhang, Y. Shi, J. Xie and F. Lei, A rapid pressureless sintering strategy for LLZTO ceramic solid electrolyte sheets prepared by tape casting, *Solid State Ionics*, 2024, **417**, 116708.

14 E. Yi, W. Wang, J. Kieffer and R. M. Laine, Flame made nanoparticles permit processing of dense, flexible, Li^+ conducting ceramic electrolyte thin films of cubic-$Li_7La_3Zr_2O_{12}$ (c-LLZO), *J. Mater. Chem. A*, 2016, **4**, 12947–12954.

15 A. C. Moy, R. L. Sacci, M. S. Chambers, A. L. Musgrove, J. Sakamoto and G. M. Veith, Irreversible Multielement Diffusion and the Resulting Compositional and Processing Flexibility in the Synthesis and Densification of Lithium Aluminum Lanthanum Zirconium Oxide, *ACS Appl. Energy Mater.*, 2025, **8**, 3003–3019.

16 S. Weinmann, H. Gobena, L. Quincke, J. J. Hinricher, S. Merk, H. Chu, T. Prein, J. L. Rupp and K. J. Kim, Stabilizing Interfaces of All-Ceramic Composite Cathodes for Li-Garnet Batteries, *Adv. Energy Mater.*, 2025, **15**, 2502280.

17 Z. D. Hood, Y. Zhu, L. J. Miara, W. S. Chang, P. Simons and J. L. Rupp, A sinter-free future for solid-state battery designs, *Energy Environ. Sci.*, 2022, **15**, 2927–2936.

18 S. Weinmann, L. Quincke, L. Winkler, J. J. Hinricher, F. Kurnia, K. J. Kim and J. L. M. Rupp, Sustainable

Functional Ceramics, *Nat. Nanotechnol.*, 2025, **20**, 1729–1745.
19 I. Bretos, R. Jiménez, J. Ricote and M. L. Calzada, Low-temperature crystallization of solution-derived metal oxide thin films assisted by chemical processes, *Chem. Soc. Rev.*, 2018, **47**, 291–308.
20 R.-J. Chen, M. Huang, W.-Z. Huang, Y. Shen, Y.-H. Lin and C.-W. Nan, Sol–gel derived Li–La–Zr–O thin films as solid electrolytes for lithium-ion batteries, *J. Mater. Chem. A*, 2014, **2**, 13277–13282.
21 Y. Zhu, Z. D. Hood, H. Paik, P. B. Groszewicz, S. P. Emge, F. N. Sayed, C. Sun, M. Balaish, D. Ehre, L. J. Miara, A. I. Frenkel, I. Lubomirsky, C. P. Grey and J. L. M. Rupp, Highly disordered amorphous Li-battery electrolytes, *Matter*, 2024, **7**, 500–522.
22 R.-J. Chen, Y.-B. Zhang, T. Liu, B.-Q. Xu, Y. Shen, Y.-H. Lin and C.-W. Nan, Improvement of the conductivity of sol-gel derived Li-La-Zr-O thin films by the addition of surfactant, *Ceram. Int.*, 2017, **43**, S603–S608.
23 S. Song, Y. Xu, Y. Ruan, H. Wang, D. Zhang, J. Thokchom and D. Mei, Isomeric Li–La–Zr–O Amorphous–Crystalline Composite Thin-Film Electrolytes for All-Solid-State Lithium Batteries, *ACS Appl. Energy Mater.*, 2021, **4**, 8517–8528.
24 T. T. Bui, B. Yun, K. Darko, S. B. Shin, J. Kim, J. Hong, M. Lee, S. K. Park and M.-G. Kim, Solution Processing of Lithium-Rich Amorphous Li-La-Zr-O Ion Conductor and Its Application for Cycling Durability Improvement of $LiCoO_2$ Cathode as Coating Layer, *Adv. Mater. Interfaces*, 2021, **8**, 2001767.
25 M. Zarabian, M. Bartolini, P. Pereira-Almao and V. Thangadurai, X-ray Photoelectron Spectroscopy and AC Impedance Spectroscopy Studies of Li-La-Zr-O Solid Electrolyte Thin Film/$LiCoO_2$ Cathode Interface for All-Solid-State Li Batteries, *J. Electrochem. Soc.*, 2017, **164**, A1133.
26 K. Tadanaga, H. Egawa, A. Hayashi, M. Tatsumisago, J. Mosa, M. Aparicio and A. Duran, Preparation of lithium ion conductive Al-doped $Li_7La_3Zr_2O_{12}$ thin films by a sol–gel process, *J. Power Sources*, 2015, **273**, 844–847.
27 M. Bitzer, T. Van Gestel, S. Uhlenbruck and H.-P. Buchkremer, Sol-gel synthesis of thin solid $Li_7La_3Zr_2O_{12}$ electrolyte films for Li-ion batteries, *Thin Solid Films*, 2016, **615**, 128–134.
28 S. Uhlenbruck, J. Dornseiffer, S. Lobe, C. Dellen, C.-L. Tsai, B. Gotzen, D. Sebold, M. Finsterbusch and O. Guillon, Cathode-electrolyte material interactions during manufacturing of inorganic solid-state lithium batteries, *J. Electroceram.*, 2017, **38**, 197–206.
29 Y. Zhu, E. R. Kennedy, B. Yasar, H. Paik, Y. Zhang, Z. D. Hood, M. Scott and J. L. M. Rupp, Uncovering the Network Modifier for Highly Disordered Amorphous Li-Garnet Glass-Ceramics, *Adv. Mater.*, 2024, 2302438.
30 J. L. Rupp, B. Scherrer and L. J. Gauckler, Engineering disorder in precipitation-based nano-scaled metal oxide thin films, *Phys. Chem. Chem. Phys.*, 2010, **12**, 11114–11124.
31 Y. Zhu, M. Chon, C. V. Thompson and J. L. M. Rupp, Time-Temperature-Transformation (TTT) Diagram of Battery-Grade Li-Garnet Electrolytes for Low-Temperature Sustainable Synthesis, *Angew. Chem., Int. Ed.*, 2023, **62**, e202304581.
32 A. Sharafi, C. G. Haslam, R. D. Kerns, J. Wolfenstine and J. Sakamoto, Controlling and correlating the effect of grain size with the mechanical and electrochemical properties of $Li_7La_3Zr_2O_{12}$ solid-state electrolyte, *J. Mater. Chem. A*, 2017, **5**, 21491–21504.
33 R. A. Jonson, E. Yi, F. Shen and M. C. Tucker, Optimization of Tape Casting for Fabrication of $Li_{6.25}Al_{0.25}La_3Zr_2O_{12}$ Sheets, *Energy Fuels*, 2021, **35**, 8982–8990.
34 "ISO 19318:2021" can be found under https://www.iso.org/standard/81448.html, accessed 11 August 2025.
35 S. Vema, F. N. Sayed, S. Nagendran, B. Karagoz, C. Sternemann, M. Paulus, G. Held and C. P. Grey, Understanding the Surface Regeneration and Reactivity of Garnet Solid-State Electrolytes, *ACS Energy Lett.*, 2023, **8**, 3476–3484.
36 H. Zhang, L. P. H. Jeurgens, C. Cancellieri, J. Sivavec, M. V. Kovalenko and K. V. Kravchyk, Standardizing XPS and HAXPES Analyses of LLZO Solid-State Electrolytes and Their Reactive Compounds, *ACS Mater. Au*, 2025, **5**, 785–797.
37 "KolXPD Software | kolibrik.net" can be found under https://www.kolibrik.net/en/solutions-products/kolxpd, accessed 19 November 2025.
38 C. R. Brundle and B. V. Crist, X-ray photoelectron spectroscopy: a perspective on quantitation accuracy for composition analysis of homogeneous materials, *J. Vac. Sci. Technol., A*, 2020, **38**, 041001.
39 J. H. Scofield, *Theoretical photoionization cross sections from 1 to 1500 keV*, 1973.
40 C. J. Powell and A. Jablonski, *NIST Electron Inelastic-Mean-Free-Path Database – Version 1.2*, National Institute of Standards and Technology, Gaithersburg, MD, 2010.
41 M. H. Brooker, Raman spectroscopic investigations of structural aspects of the different phases of lithium sodium and potassium nitrate, *J. Phys. Chem. Solids*, 1978, **39**, 657–667.
42 N. Zhang, G. Ren, L. Li, Z. Wang, P. Yu, X. Li, J. Zhou, H. Zhang, L. Zhang, Z. Liu and X. Liu, Dynamical evolution of CO_2 and H_2O on garnet electrolyte elucidated by ambient pressure X-ray spectroscopies, *Nat. Commun.*, 2024, **15**, 2777.
43 G. Larraz, A. Orera and M. L. Sanjuán, Cubic phases of garnet-type $Li_7La_3Zr_2O_{12}$: the role of hydration, *J. Mater. Chem. A*, 2013, **1**, 11419–11428.
44 F. Tietz, T. Wegener, M. T. Gerhards, M. Giarola and G. Mariotto, Synthesis and Raman micro-spectroscopy investigation of $Li_7La_3Zr_2O_{12}$, *Solid State Ionics*, 2013, **230**, 77–82.
45 K. J. Kim and J. L. M. Rupp, All ceramic cathode composite design and manufacturing towards low interfacial resistance for garnet-based solid-state lithium batteries, *Energy Environ. Sci.*, 2020, **13**, 4930–4945.
46 A. Orera, G. Larraz and M. L. Sanjuán, Spectroscopic study of the competition between dehydration and carbonation

effects in La_2O_3-based materials, *J. Eur. Ceram. Soc.*, 2013, **33**, 2103–2110.

47 R. Flammang, N. Dechamps, P. Gerbaux, P.-C. Nam and M. T. Nguyen, Unimolecular chemistry of metastable dimethyl isophthalate radical cations, *Int. J. Mass Spectrom.*, 2008, **275**, 110–116.

48 H. Monia, Z. Hmida and K. Ismail, Heat capacities and enthalpies of fusion of lithium and rubidium nitrates: heat capacities, enthalpies of fusion and enthalpies of formation of the intermediate compounds $Ag_{0.5}Rb_{0.5}NO_3$ and $Li_{0.5}Rb_{0.5}NO_3$, *Thermochim. Acta*, 2013, **568**, 204–208.

49 D. R. Baer, K. Artyushkova, H. Cohen, C. D. Easton, M. Engelhard, T. R. Gengenbach, G. Greczynski, P. Mack, D. J. Morgan and A. Roberts, XPS guide: charge neutralization and binding energy referencing for insulating samples, *J. Vac. Sci. Technol., A*, 2020, **38**, 031204.

50 N. Zhang, G. Ren, L. Li, Z. Wang, P. Yu, X. Li, J. Zhou, H. Zhang, L. Zhang, Z. Liu and X. Liu, Dynamical evolution of CO_2 and H_2O on garnet electrolyte elucidated by ambient pressure X-ray spectroscopies, *Nat. Commun.*, 2024, **15**, 2777.

51 H. Zhang, G. Paggiaro, F. Okur, J. Huwiler, C. Cancellieri, L. P. H. Jeurgens, D. Chernyshov, W. van Beek, M. V. Kovalenko and K. V. Kravchyk, On High-Temperature Thermal Cleaning of $Li_7La_3Zr_2O_{12}$ Solid-State Electrolytes, *ACS Appl. Energy Mater.*, 2023, **6**, 6972–6980.

52 S. Vema, F. N. Sayed, S. Nagendran, B. Karagoz, C. Sternemann, M. Paulus, G. Held and C. P. Grey, Understanding the Surface Regeneration and Reactivity of Garnet Solid-State Electrolytes, *ACS Energy Lett.*, 2023, **8**, 3476–3484.

53 M. Pokhrel, M. Alcoutlabi and Y. Mao, Optical and X-ray induced luminescence from Eu^{3+} doped $La_2Zr_2O_7$ nanoparticles, *J. Alloys Compd.*, 2017, **693**, 719–729.

54 C. Kaliyaperumal, S. K. Marndi, A. Sankarakumar and T. Paramasivam, Physical insights into the grain size effect on the electrical properties of nanocrystalline $La_2Zr_2O_7$ pyrochlores, *Ceram. Int.*, 2023, **49**, 10663–10672.

55 S. Wang, H. Chiu and G. P. Demopoulos, Tetragonal phase-free crystallization of highly conductive nanoscale cubic garnet ($Li_{6.1}Al_{0.3}La_3Zr_2O_{12}$) for all-solid-state lithium-metal batteries, *J. Power Sources*, 2024, **595**, 234061.

56 Y.-T. Chen, A. Jena, W. K. Pang, V. K. Peterson, H.-S. Sheu, H. Chang and R.-S. Liu, Voltammetric Enhancement of Li-Ion Conduction in Al-Doped $Li_{7-x}La_3Zr_2O_{12}$ Solid Electrolyte, *J. Phys. Chem. C*, 2017, **121**, 15565–15573.

57 Z. Tan, S. Li, F. Wang, D. Qian, J. Lin, J. Hou and Y. Li, High performance polymer solar cells with as-prepared zirconium acetylacetonate film as cathode buffer layer, *Sci. Rep.*, 2014, **4**, 4691.

58 A. Kotani, M. Okada, T. Jo, A. Marcelli and J. C. Parlebas, Many Body Effect in Inner Shell Photoemission and Photoabsorption Spectra of La Compounds, *J. Phys. Soc. Jpn.*, 1987, **56**, 798–809.

59 M. F. Sunding, K. Hadidi, S. Diplas, O. M. Løvvik, T. E. Norby and A. E. Gunnæs, XPS characterisation of *in situ* treated lanthanum oxide and hydroxide using tailored charge referencing and peak fitting procedures, *J. Electron Spectrosc. Relat. Phenom.*, 2011, **184**, 399–409.

